Operando Entropy Profiling of Sodium-Ion Batteries via Optical Fiber Sensing for Thermal Management and Ageing Monitoring

Jiaqiang Huang, Charles Delacourt, Parth Desai, Jean-Marie Tarascon

Journal of The
Electrochemical Society

OPEN ACCESS

Operando Entropy Profiling of Sodium-Ion Batteries via Optical Fiber Sensing for Thermal Management and Ageing Monitoring

To cite this article: Jiaqiang Huang *et al* 2024 *J. Electrochem. Soc.* **171** 030516

Journal of The Electrochemical Society, 2024 **171** 030516

Operando Entropy Profiling of Sodium-Ion Batteries via Optical Fiber Sensing for Thermal Management and Ageing Monitoring

Jiaqiang Huang,[1,2,3,4] Charles Delacourt,[4,5] Parth Desai,[1,4,6] and Jean-Marie Tarascon[1,4,6,z]

[1]*Collège de France, Chimie du Solide et de l'Energie—UMR 8260 CNRS, Paris, France*
[2]*The Hong Kong University of Science and Technology (Guangzhou), Sustainable Energy and Environment Thrust and Guangzhou Municipal Key Laboratory of Materials Informatics, Nansha, Guangzhou, Guangdong 511400, People's Republic of China*
[3]*HKUST Shenzhen-Hong Kong Collaborative Innovation Research Institute, Futian, Shenzhen, Guangdong, People's Republic of China*
[4]*Réseau sur le Stockage Electrochimique de l'Energie (RS2E), CNRS FR 3459, Hub de l'Energie, Rue Baudelocque, 80039 Amiens Cedex, France*
[5]*Laboratoire de Réactivité et Chimie des Solides (LRCS), CNRS UMR 7314, Université de Picardie Jules Verne, Hub de l'Energie, Rue Baudelocque, 80039 Amiens Cedex, France*
[6]*Sorbonne Université, 4 Place Jussieu, Paris 75005, France*

Batteries are essential for the electrification of transport and the replacement of internal combustion engines. Thermodynamics was largely established with the development of the engines, and this knowledge has been applied to batteries for years. In particular, entropy profiles are sensitive to structural changes and are useful for diagnosing and understanding battery ageing. However, entropy profiling of aged batteries is mainly limited to the potentiometric method, which makes the technique in situ and time-consuming. Herein, we rely on optical fiber calorimetry to perform operando entropy profiling of commercial sodium-ion cells. Firstly, we directly compare the entropy profile of sodium-ion $Na_3V_2(PO_4)_2F_3$/hard carbon (NVPF/HC) chemistry against those of commercialized lithium-ion chemistries, highlighting the uniqueness of NVPF/HC chemistry in battery thermal management. Operando entropy profiling of NVPF/HC chemistry further elucidates the structural degradations that take place during cycling and provide features that can be important indicators of the battery's state of health. This work reintroduces thermodynamic analyses as a valuable tool for batteries and spotlights the new horizons offered by the convergence of battery sensing, thermodynamics, and other disciplines.

 [DOI: 10.1149/1945-7111/ad30da]

Manuscript submitted December 23, 2023; revised manuscript received February 27, 2024. Published March 15, 2024.

Supplementary material for this article is available online

Batteries currently play a crucial role in the electrification of transport, the storage of renewable yet intermittent energies, and in the power sources of various consumer electronics. However, concerns about the sustainability of batteries have increased due to the upcoming retirement of tons of batteries.[1,2] Is it possible to extend the life of batteries and delay their disposal? The answer to this question is linked to the degradation of batteries, i.e., the reduction in performance over time as a result of differences between battery properties and their pristine state. Consequently, the know-how to monitor and control the varying properties of the batteries becomes the essential key to a more lasting and sustainable battery.

There is currently a growing number of ways of characterizing a battery's properties over the course of its life. To name a few, X-rays can help to perceive the evolution of the crystalline structure of active materials by X-ray diffraction (XRD) and three-dimensional spatial structure by X-ray computed tomography (XCT). Scanning electron microscopy (SEM) and transmission electron microscopy (TEM) are frequently used to visualize the morphological changes in active materials or at interphases after ageing tests. In addition to these major techniques, thermodynamic analyses have long been applied to study the properties of battery systems. Prior to the battery, the heat generated by electrochemical reactions had been measured by calorimetry[3] since 1958. In 1978, Gibbard et al. calculated the enthalpy and entropy of lead-acid batteries and the thermal efficiencies of several battery systems.[4] With regard to lithium intercalation chemistry, in 1985, Dahn et al. used calorimetric methods[5] to detect the distribution of intercalation atoms in $Li_xMo_6Se_8$ via the variation of entropy. In 2006, Yamada et al. detected the room-temperature miscibility gap in Li_xFePO_4 via a configurational entropy anomaly.[6] Our group also used isothermal calorimetry in 2019 to probe the thermal effects of voltage hysteresis in lithium-rich cathodes based on anionic redox with detailed analyses of enthalpy potentials.[7]

Thermodynamic analyses are indeed useful for understanding the ageing behavior of batteries. For example, in 2014, Yazami et al. showed the greater sensitivity of entropy and enthalpy state functions rather than the Gibbs free energy associated with variations of the crystalline structure of $LiCoO_2$/C chemistry, resulting from cycling ageing (up to 1,000 cycles).[8] Subsequently, in 2019, Choi et al. studied the entropy profiles of $LiCoO_2$ with and without Ni doping to detect and compare their structural evolutions before and after 50 cycles.[9] Later on, Choi et al. extended their analyses to high-nickel layered oxide cathodes and showed that microcracks in cathode particles could be detected after 100 cycles via entropy changes.[10] Meanwhile, Mercer et al. also exploited the entropy profiles to diagnose the degradations of graphite-silicon composite anodes after cycling and calendar ageing.[11] The above studies demonstrated the versatility and generalizability of thermodynamic tools (in particular entropy profiles) for detecting the degradation of different electrode chemistries, including layered oxides, graphite, and silicon electrodes.

Coincidently, the above studies of ageing-related entropy[8–11] were all based on the potentiometric method, which centers around the following equation[8,9] from the Maxwell relation.[5]

$$\left(\frac{\partial s}{\partial x}\right)_p = nF\left(\frac{\partial U}{\partial T}\right)_p \quad [1]$$

where s is the molar entropy of the cell (unit: J K^{-1} mol^{-1}), x is the intercalation number of materials (such as x in $Na_xV_2(PO_4)_2F_3$), p is

[z]E-mail: jean-marie.tarascon@college-de-france.fr

the pressure, T is the temperature (K), n is the electron number involved in the electrochemical reaction ($n = 1$ for lithium- and sodium-ion batteries), F represents the Faraday's constant (96 485 C mol^{-1}), and U is the equilibrium potential (V; frequently estimated by the open-circuit voltage, OCV, after relaxation). Given Eq. 1, the potentiometric method is easy to implement, requiring a potentiostat to measure U and a thermal chamber to vary T. However, the method is time-consuming.

The calorimetric method is based on the equation describing the energy balance of the battery system (ignoring the enthalpy of mixing),[12]

$$\dot{Q} = I(V - U) + \frac{IT}{nF}\left(\frac{\partial s_+}{\partial x} - \frac{\partial s_-}{\partial x}\right) + \dot{q}_P \qquad [2]$$

where $\dot{Q}$ represents the heat generation rate of the battery (W), I represents the current (A), V represents the voltage (V), $\frac{ds_+}{dx}$ and $\frac{ds_-}{dx}$ represent the change rates of molar entropy of the positive and negative electrodes (J K^{-1} mol^{-1}), respectively,[7,13,14] $\dot{q}_P$ represents the parasitic heat rate (W). Equation 2 can be transformed into

$$\frac{\partial s}{\partial x} = \left(\frac{\partial s_+}{\partial x} - \frac{\partial s_-}{\partial x}\right) = [\dot{Q} - I(V - U) - \dot{q}_P]\frac{nF}{IT} \qquad [3]$$

Without varying T of the thermal chamber, the calorimetric method requires a calorimeter to measure $\dot{Q}$ as well as some assumptions[5,15,16] or measurements[12] to obtain U and $\dot{q}_P$. The potentiometric or calorimetric methods rely on different experimental setups. The predominance of the potentiometric method across the literature for ageing studies[8–11] is probably because of the simpler and more available experimental setup, as it is difficult to book a calorimeter (which can be costly) for long-term experiments. Nevertheless, the weaknesses of the potentiometric method lie in the following facts: (1) It takes time to vary T and measure U with 3.5 to 30 h[9–11] for each entropy data point; (2) The limited number of data points sacrifices the resolution; (3) It cannot estimate entropy in real time, making the technique in situ rather than operando. Facing these weaknesses, it becomes intriguing to explore the application of the calorimetric method in the study of ageing.

So how to obviate the use of classical calorimetry for long-term ageing experiments? We previously derived a method based on optical fibers used as temperature sensors to indirectly estimate the rate of heat generation and eventually derive the entropy and enthalpy state functions.[12,17] On the other hand, we used tilted fiber Bragg grating sensors to monitor battery ageing after 100 cycles,[18] demonstrating the feasibility of long-term measurements with optical fiber sensors. In short, our previous studies[12,17–22] on optical fiber battery sensors pave the way for operando profiling of cell reaction entropy upon long-term ageing.

Herein, we select sodium-ion 18650 $Na_3V_2(PO_4)_2F_3$/hard carbon (NVPF/HC) commercial batteries as our model system, thus extending the previously mentioned thermodynamic studies[8–11] on the ageing of Li-ion batteries to the ageing of sodium-ion batteries. Our manuscript is structured as follows. We first recall the basic definitions of entropy and discuss the reported relationships between entropy and intercalation mechanisms. Based on optical fiber calorimetry, we then present the operando entropy profiles of NVPF/HC cells during cycling and decode structural degradations. Finally, we show the strong correlation between entropy features and battery states, suggesting the potential of entropy as a descriptor of battery state of health.

Experimental

NVPF/HC 18650 cells.—TIAMAT (France) kindly supplied the cells, which were produced and hermetically sealed before being filled with electrolytes. To fill the electrolyte in our lab and insert the internal sensor, a hole of 0.8-mm was drilled on the central position of the negative pole of the cells. Note that a void is present in the center of the jelly roll arising from the fabrication. Afterwards, these cells were dried in a glass vacuum oven (Buchi) at 80 °C overnight to remove the air and possible moisture in the cell. The dried cells were transferred into an Ar-filled glovebox without air exposure.

Electrolyte.—To study cyclic ageing, we select a relatively high-performance electrolyte for 18650 cells with the same electrolyte additives as reported previously.[23] The electrolyte consisted of contains 1 M $NaPF_6$ in ethylene carbonate (EC) and dimethyl carbonate (DMC) (v.:v. = 1:1) with 3 wt% vinylene carbonate (VC), 3 wt% succinonitrile (SN), 0.5 wt% sodium (oxalate) difluoro borate (NaODFB), and 0.2 wt% tris(trimethylsilyl) phosphite (TMSPi). The solvents for the electrolyte, including those for coin cells, namely, sulfolane (99%, Sigma Aldrich), fluoroethylene carbonate (FEC, >98%, TCI chemicals), and diglyme (99.5%, Sigma Aldrich), were dried over molecular sieves (4 Å) for three days, and the water content of less than ten ppm was verified by Karl-Fisher titration. Salts were loaded into a glass oven (BÜCHI, Germany) in the glove box, taken out to be dried under a vacuum at 80 °C, and finally transferred back to the glove box without exposure to the air.

Fiber Bragg grating (FBG) sensors.—We purchased the FBG sensors from SAMYON (China). The 10-mm grating was written in single-mode silica fibers. All the FBG sensors were calibrated in the temperature-programmable oven from 55 to 45 °C in 5 °C decrements to get their temperature sensitivity in the unit of pm $°C^{-1}$. A few examples of calibration were presented elsewhere.[12,18]

Sensor integration.—In the Ar-filled glovebox, the as-prepared electrolyte was injected into the as-dried 18650 cells through the 0.8 mm hole until 5.5 ml was reached. Afterwards, FBG sensors were inserted into the 18650 cells through the 0.8 mm hole as well and finally resided in the central void of the jelly roll. Epoxy was applied to ensure the air tightness of the cell. After overnight curing, these cells were taken out of the glove box for further measurements.

Electrochemical and optical measurements.—We tested the 18650 and coin cells with potentiostat (Bio-Logic, France) in a temperature-controllable chamber (Memmert, Germany). As for FBG sensors, we used an interrogator (Si255, Micron Optics, U.S.) as the light source and the wavelength detector. Given the specification of the interrogator, the wavelength accuracy and resolution were 1 pm, corresponding to ∼0.1 °C for the sensor. The acquisition time was set as 1 Hz rather than 1,000 Hz to reduce the size of the data.

Optical fiber calorimetry.—We used the same setup that we reported previously.[12] After being taken out of the glove box, the 18650 cells were placed in standard cabinets to ensure consistency between different cells. In addition to the internal FBG sensor as integrated (i.e., internal sensor), another two FBG sensors were put on the surface of the cell (i.e., surface sensor) and the inner wall of the cabinet (i.e., ambient sensor), respectively. Note that a tiny Kapton tape was applied next to the FBG region to ensure the closeness between the FBG and the cell surface. In this setup, these three sensors measured the internal ($T_{internal}$), surface ($T_{surface}$), and ambient ($T_{ambient}$) temperatures, respectively. A simplified zero-dimensional model[24] was adopted to calculate the temporal heat generation rate ($\dot{Q}$) of the cells,

$$\dot{Q} = MC_P\frac{dT}{dt} + \frac{T_{surface} - T_{ambient}}{R_{out}} \qquad [4]$$

where M is the cell's mass, C_P is the specific heat capacity, T is the spatial average temperature of the cell calculated[12] by $T_{internal}$ and $T_{surface}$ together with the cell geometry, t is the time, and R_{out} is the equivalent thermal resistance between the cell's surface and the ambient surrounding. Among these parameters, MC_P and R_{out} were

determined by the transient and steady states during the thermal pulses, respectively (see the details elsewhere).[12] We assumed the MC_P and R_{out} were constant within the temperature range of the measurement. With the operando temperature measurement, the temporal heat generation rate ($\dot{Q}$) could be computed according to Eq. 4.

Operando entropy estimation by the calorimetric method.—The operando entropy measurements were based on Eq. 3. In this work, $\dot{Q}$ was estimated by the optical fiber calorimeter[12] while I and V were monitored by potentiostat. Regarding U, it can be either estimated by the average voltage of charge and discharge or obtained by the galvanostatic intermittent titration technique (GITT). In this work, we selected the GITT to get the U as previously.[12] To suppress the artifact arising from the linear interpolation of OCV as seen previously,[12] the shape-preserving piecewise cubic interpolation was adopted instead; see more details in Fig. S1. Note that more OCV points (particularly at the voltage-fast-varying regions) could indeed further suppress the artifacts from interpolations; however, the extended experimental time may exacerbate the self-discharge. To eliminate this interpolation-induced artifact, the average voltage of charge and discharge curves can also be directly used as the equilibrium voltage as Dahn et al. did,[16] which is, however, based on a strong assumption: No asymmetric reaction pathway during the charge and discharge. We therefore adhered to GITT in this work. Besides, to account for the varying U with state of health (SOH), GITT tests were conducted every 20 cycles except for the initial ones; see elsewhere.[17] In this work, we also ignored the $\dot{q}_P$, which was proved to be a reasonable assumption in our previous work.[17] Afterwards, the entropy can be computed according to Eq. 3.

Ageing protocols of 18650 cells.—The cabinets were placed in a 55 °C thermal chamber. The formation of cells was done at C/10 (1 C = 128 mA g_{NVPF}^{-1}) for 3 cycles. Afterwards, the cells were charged at 1 C with a constant current—constant voltage (CC-CV, CV to C/5) and discharged at the constant current of 1 C within the voltage window of 2.0–4.25 V. Diagnostic cycles, consisting of GITT and the 5 C discharge, were conducted every 20 cycles except for the initial ones.

Coin cell preparation.—For the measurements of coin cells at 25 °C-30 °C-35 °C, 1 M $NaPF_6$ in diglyme was used for both HC and NVPF half cells. For 55 °C-50 °C-45 °C measurements, 1 M $NaPF_6$ in diglyme and 1 M NaTFSI in sulfolane-FEC (7:3 by volume) were used for HC and NVPF half cells, respectively, for minimizing the side reactions. The electrolyte combinations were screened according to cyclic stability at C/5 and polarization at 1 C. NVPF and HC coated on Al foil were received from Tiamat, France. The electrodes were specially coated only on one side of the Al foil for conducting the studies in coin cells. All of the electrodes were dried in a Buchi oven under vacuum (lower than 100 mbar) at 100 °C for 12 h prior to being transferred into the glove box. The electrochemical performance of half cells was evaluated in 2032-type coin cells separated by two layers of glass fiber containing 200 μl of desired electrolytes. The experiments were reproduced for two sets of cells to confirm the phenomenon.

Half-cell entropy profiles by the potentiometric method.—To estimate the entropy profiles of the NVPF/Na and HC/Na coin cells, Eq. 1 was adopted because the temperature changes of our coin cells were too small to be detected by FBG sensors. Consequently, the entropy change of the reaction, $\Delta S(x)$, can be calculated if the temperature dependence of $U(x)$ is known. In practice,[25–28] $U(x)$ was measured and estimated by the OCVs after long relaxations at different temperatures. It frequently took 3.5 to 30 h[9–11] to reach the quasi-equilibrium state at each temperature and state of charge (SOC) state, which is substantially time-consuming. To reduce the experimental time, we followed the methodology developed by Osswald et al.[29] to shorten the relaxation time down to 30 min at each temperature by background subtraction.

To conduct OCV measurements at 25 °C-30 °C-35 °C, one formation cycle was performed for both NVPF and HC half cells at 25 °C. The charging protocol involved charging at a rate of 1 C for 3 min, followed by a 3-hour rest at OCV with a temperature sequence consisting of 1 h and 30 min at 25 °C, 30 min at 30 °C, 30 min at 35 °C, and 30 min at 25 °C. After 20 rounds of 1 C charging for 3 min each, to recover any capacity lost due to self-discharge during the OCV periods, 2 rounds of C/5 charging for 15 min were conducted with the same temperature sequence during the OCV periods. The same C-rate variations, OCV resting periods, and temperature sequence during OCV resting periods were applied during the discharge protocol of both NVPF and HC cells.

For OCV measurements at 55 °C-50 °C-45 °C, a formation cycle was carried out for both NVPF and HC half cells at 55 °C. The charging and discharging protocols were kept identical to those used for the measurements at 25 °C-30 °C-35 °C, except for the temperature sequence during the OCV resting periods. Specifically, the OCV resting periods involved a 3-h rest at OCV with a temperature sequence consisting of 1 h and 30 min at 55 °C, followed by 30 min at 50 °C, 30 min at 45 °C, and 30 min at 55 °C. It should be noted that the cells are expected to relax at a faster pace than those held at 25 °C-30 °C-35 °C. However, self discharge is also expected to be larger. Usually, the OCV period is adjusted as a tradeoff between reaching equilibrium whilst minimizing self discharge. However, in this study, we refrained from complicating the measurements because the coin-cell measurements were intended solely for reference purposes.

Retrospective on Entropy of Intercalation Compounds

Overview.—Before analysing the entropy profile, we shall revisit the fundamental relationship between entropy and intercalation chemistry in order to investigate the underlying phenomena that cause cell ageing. Entropy is an interesting, extensive property and a state function of the battery system. But what does entropy mean? In classical thermodynamics or, more precisely, in the Second Law of Thermodynamics,[30] the entropy (S; in J K^{-1}) of a system is defined as follows.

$$dS = \frac{\delta q_{rev}}{T} \quad [5]$$

where δq_{rev} is the incremental thermal energy (unit: J) that has been reversibly added (or expelled). Apparently, $\frac{IT}{nF}\left(\frac{\partial s_+}{\partial x} - \frac{\partial s_-}{\partial x}\right)$ in Eq. 2 is a transformation of $\delta q_{rev} = TdS$ in Eq. 5 considering the electrochemical reactions. Nevertheless, the physical meaning of entropy is not easy to understand within the framework of classical thermodynamics.[30] Turning to statistical mechanics, a famous physical description of entropy by Gibbs is the "degree of mixed-up-ness" of a system at the atomic or molecular level.[30] This "degree of mixed-up-ness" can be further quantified by the Boltzmann's equation:[30]

$$S = k \ln \Omega \quad [6]$$

where k is the Boltzmann constant (1.38×10^{-23} J K^{-1}), and Ω is the number of ways (or called microstates) in which the system's energy can be distributed. The consideration of energy distribution can further decompose entropy into two parts, including the configurational entropy (S_{conf}) and the thermal entropy (S_{th}).[30]

Configurational entropy.—The configurational entropy is correlated to the number of ways to distribute the particles in the available space (Ω_{conf}). More precisely, in the battery materials, researchers (Dahn,[31] Fultz,[32] Mercer,[33] Gasteiger[34]) consider Ω_{conf} mainly implies the number of ways in which the intercalants (such as

sodium/lithium ions) or vacancies can be arranged within the host structure (such as NVPF). Mathematically, the variation of S_{conf} can be described by the following equations thanks to the point approximation[9,32] of intercalants and vacancies:

$$S_{conf} = -k(x_2 - x_1)[\chi \ln\chi + (1-\chi)\ln(1-\chi)] \quad [7]$$

$$\chi = \frac{x - x_1}{x_2 - x_1} \quad [8]$$

where, x_1 and x_2 are the equilibrium compositions, that is, the boundaries of the miscibility gap, and $x_1 < x < x_2$. If one considers a compound where all insertion sites are identical, such as $LiFePO_4$, then x_1 and x_2 must be zero and one, respectively. To be consistent with what could be measured experimentally through Eqs. 1 or 3, the derivative of molar configurational entropy ($s_{conf} = N_A S_{conf}$, where N_A is the Avogadro constant, 6.02×10^{23} mol^{-1}) can be computed:

$$\frac{\partial s_{conf}}{\partial x} = R \ln\left(\frac{x_2 - x}{x - x_1}\right) \quad [9]$$

where R is the gas constant, 8.314 J K^{-1} mol^{-1}, equivalent to kN_A. To provide readers with an intuition of the shapes of s_{conf} and $\frac{\partial s_{conf}}{\partial x}$, we plotted the Eqs. 7 and 9 in Figs. 1a, 1b, respectively. From the figure, we can see the curve of s_{conf} as a function of x has a bell-like shape, while $\frac{\partial s_{conf}}{\partial x}$ is monotonic with x. The interactions between the neighbor intercalants or vacancies are nearly zero at infinite dilution of Li or vacancy. However, once the interaction becomes significant, the interaction terms[33,35] should be added to the model. In that case, the $\frac{\partial s_{conf}}{\partial x}$ can be non-monotonic, see examples elsewhere.[9,33,35]

Thermal entropy.—Meanwhile, battery researchers generally divide the thermal entropy into electronic (S_{elec}) and vibrational (S_{vib}) entropies,[32–34] corresponding to thermal disorder in electronic states near the Fermi level and vibrational frequency in the crystal lattice, respectively. Furthermore, S_{elec} and S_{vib} do vary with the (de-) intercalation. For example, the Mott transition in Li_xCoO_2 is accompanied by a considerable change[32] of S_{elec}, because the insulating phase of Li_xCoO_2 at $x > 0.95$ has a zero S_{elec}. Besides, Gasteiger et al. ascribed a broad peak of $\frac{\partial s}{\partial x}$ to the phase transition in lithium- and manganese-rich layered transition metal oxides ($Li_{1.14}[Ni_{0.26}Co_{0.14}Mn_{0.6}]_{0.86}O_2$), which largely modified S_{vib}.[35] In addition to phase transitions, Dahn et al.[31] and Fultz et al.[32] also identified the variation of S_{th} (or molar thermal entropy, s_{th}) in mono-phasic solid solution reactions by comparing the theoretical $\frac{\partial s_{conf}}{\partial x}$ computed from Eq. 9 with the experimental $\frac{\partial s}{\partial x}$ profiles. They found that $\frac{\partial s_{th}}{\partial x}$ could be taken as constant offsets in either $Li_xMo_6Se_8$[31] or Li_xCoO_2,[32] which then became a frequently used assumption for entropy studies.[10,31–33] Consequently, we consider the S_{th} (including both S_{elec} and S_{vib}) as a whole and take the same assumption that $\frac{\partial s_{th}}{\partial x}$ only offer a constant offset. Note that S_{elec} and S_{vib} could be calculated by complementary density functional theory computation and neutron scattering, respectively; see Fultz's papers.[32,36] It is therefore possible to estimate the contributions[31] of S_{elec}, S_{vib}, and S_{conf}, respectively, though which is beyond the scope of this work.

First-order phase transition.—McKinnon et al. studied[31] the correlation between $\frac{\partial s}{\partial x}$ and phase transitions in $Li_xMo_6Se_8$. They found that the first-order phase transitions could induce plateaus,[31] which was rationalized by the entropy jump in the phase transition. See the following equation:[31]

$$\left(\frac{\partial s}{\partial x}\right)_{x_1,x_2} = \frac{s_\alpha(x_1) - s_\beta(x_2)}{x_1 - x_2} \quad [12]$$

where $s_\alpha(x_1)$ and $s_\beta(x_2)$ are the molar entropies of phases α and β at the boundaries of the miscibility gap, $x = x_1$ and $x = x_2$, respectively. From the equation, the $\frac{\partial s}{\partial x}$ of the first-order phase transition can be constant in the two-phase coexistence region (or called miscibility gap[6]) with the discontinuity at the equilibrium compositions (green arrows, Fig. 1d), leading to the plateau shape of $\frac{\partial s}{\partial x}$ curve[6,31] (Fig. 1d). According to McKinnon's paper,[31] those discontinuities of $\frac{\partial s}{\partial x}$ are proportional to the change in x_i ($i = 1$ or 2) with temperature. Moreover, when batteries are (dis-)charged at the non-zero intercalation rate, two neighbor transitions could coexist at the boundaries, smearing the $\frac{\partial s}{\partial x}$ features[31] (Fig. 1d). For

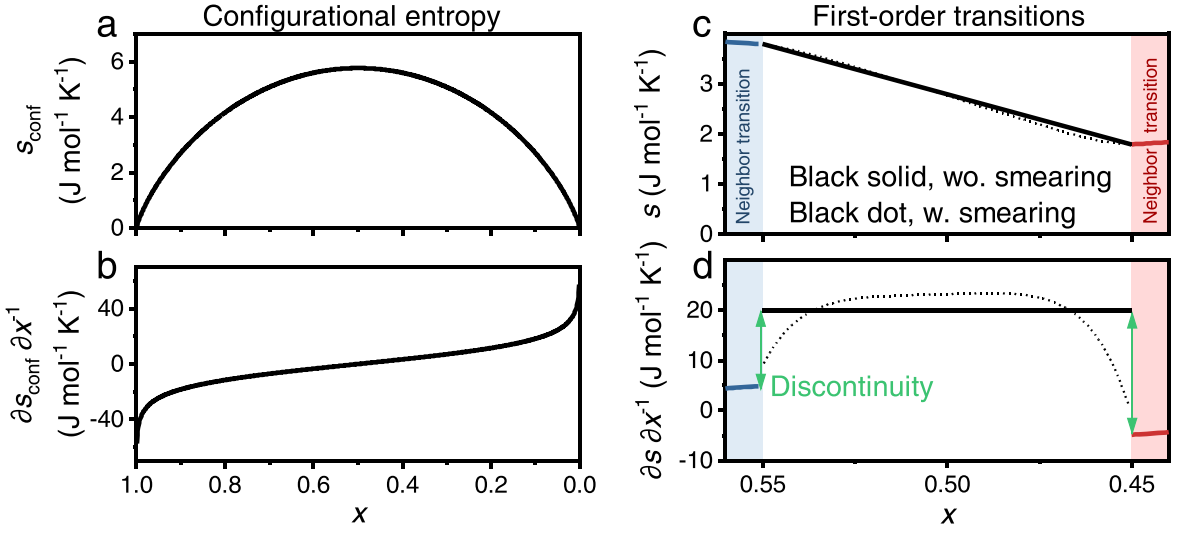

Figure 1. Schematic entropy profiles for intercalation compounds. a,b, The theoretical curve of molar configurational entropy (s_{conf}, a) and the derivative of s_{conf} with respective to x (that is, $\frac{\partial S_{conf}}{\partial x}$, b) as a function of the intercalation number (x) between the equilibrium compositions according to Eqs. 7 and 9, respectively. c,d, The schematic curve of molar entropy (s, **c**) and its derivative with respect to x ($\frac{\partial s}{\partial x}$, d) as a function of x without (black solid) and with (black dot) considering the smearing effects[31] from the neighbor transitions (blue and red regions). The discontinuities are marked by green arrows.

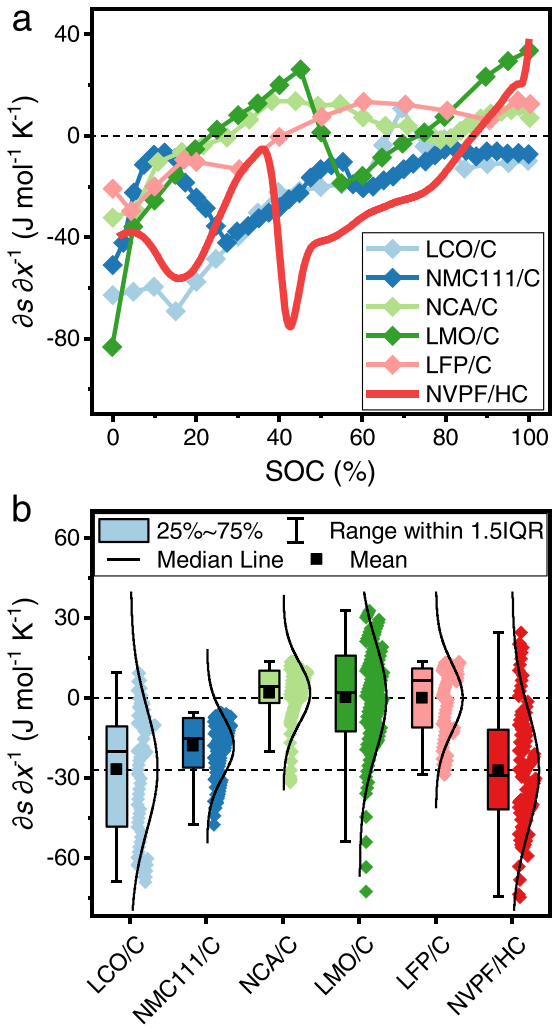

Figure 2. Entropy comparison between lithium- and sodium-ion chemistries. a, Comparison of entropy profiles of $LiCoO_2$/C ("LCO/C"),[37] $LiNi_{1/3}Mn_{1/3}Co_{1/3}O_2$/C ("NMC111/C"),[29] $LiNi_{0.8}Co_{0.15}Al_{0.05}O_2$/C ("NCA/C"),[29] $LiMn_2O_4$/C ("LMO/C"),[37] $LiFePO_4$/C ("LFP/C"),[38] and NVPF/HC (data from the 12th charge) chemistries. Note that the lithium-ion data was retrieved from literature.[29,37,38] b, Statistic analyses of a by box plots (left) together with the normal distributions (right) of the data. As described in the legend, the box covers the data within the first and third quartile, while the whiskers indicate the range within the 1.5 interquartile range (IQR). Meanwhile, the short horizontal bars and squares represent the median and mean values of the data. To get rid of the uneven SOC sampling in a, the data were interpolated with the same SOC sequence in b. Data in a adapted with permission from: LCO/C, Ref. 37, Elsevier; NMC111/C, Ref. 29, Elsevier; NCA/C, Ref. 29, Elsevier; LMO/C, Ref. 37, Elsevier; LFP/C, Ref. 38, Elsevier.

higher-order transitions such as order-disorder transitions, the discontinuity of $\frac{\partial s}{\partial x}$ can also occur, see McKinnon's paper.[31]

Results

Comparing entropies of lithium- and sodium-ion chemistries.— Since entropy changes are important to the battery thermal management,[37] we recalled the entropy results of lithium-ion chemistries (data from literature[29,37,38]) and plotted them against our results of NVPF/HC sodium-ion chemistry (at 12th charge) in Fig. 2. Note that Damay et al.[39] have previously reported the entropy profiles of NVPF/HC. By comparison in Fig. S2, we found that our entropy profiles are mostly consistent with that of Damay et al.[39] with more delicate features owing possibly to the internal optical fiber sensor used in this work and the different experimental setups.

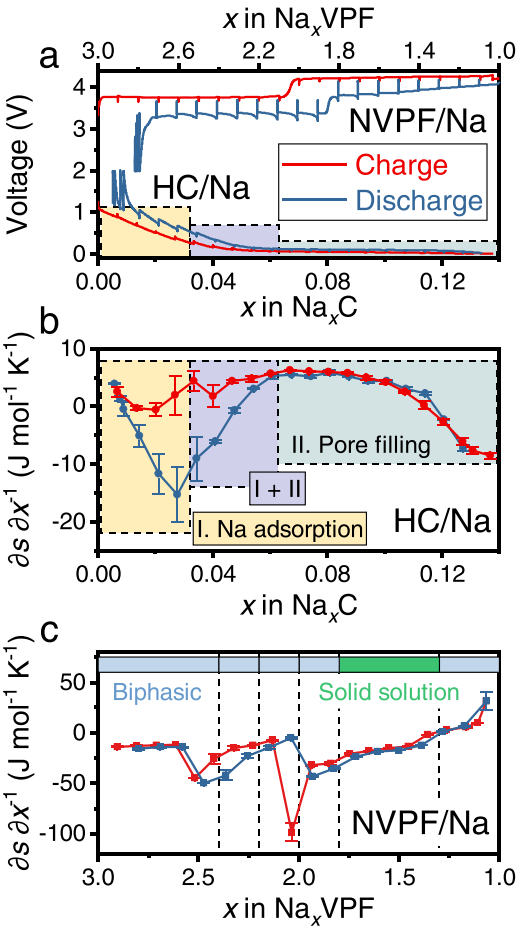

Figure 3. Half-cell entropy profiles computed by potentiometric methods. a, Voltage profiles of NVPF/Na and HC/Na half cells during the charge (red) and discharge (blue) in a 55 °C oven for the entropy estimation; see details in Experimental. **b,c,** The computed HC/Na (**b**) and NVPF/Na (**c**) entropy profiles during the charge (red) and discharge (blue). The self-discharge effect on NVPF/Na was corrected; see Fig. S4. Error bars are computed by the standard errors of the coefficient in the linear fitting of Eq. 1. The phase diagram[43] of NVPF from the operando synchrotron XRD was attached in **c** as a reference. Because the 18650 cells were cycled in a 55 °C oven and entropy profiles are functions of temperature, the coin-cell results at the same temperature were chosen here for the consistency and later comparison purposes.

Figure 2a shows that the entropy ($\frac{\partial s}{\partial x}$) profile of NVPF/HC is negative in SOC $<$ 85%, with a narrow positive region in SOC $>$ 85%. This indicates that, in SOC $<$ 85%, the NVPF/HC cells offer endothermic cooling and exothermic heating via the entropy changes during the charge and discharge, respectively.[39] More importantly, the magnitude of entropic heat of NVPF/HC is similar to that of $LiCoO_2$/C chemistry[37] and more prominent than other lithium-ion chemistries, including $LiNi_{1/3}Mn_{1/3}Co_{1/3}O_2$/C,[29] $LiNi_{0.8}Co_{0.15}Al_{0.05}O_2$/C,[29] $LiMn_2O_4$/C,[37] and $LiFePO_4$/C.[38]

For a more quantitative comparison, we performed the statistical analyses on the entropy profiles of different chemistries by box plots and normal distributions in Fig. 2b. The mean entropy change of NVPF/HC cell (ca. -27 J mol^{-1} K^{-1}) is almost identical to that of $LiCoO_2$/C cell and lower than other cells ($LiNi_{1/3}Mn_{1/3}Co_{1/3}O_2$/C $<$ $LiMn_2O_4$/C $\approx$ $LiFePO_4$/C $\approx$ $LiNi_{0.8}Co_{0.15}Al_{0.05}O_2$/C $\approx$ 0). Meanwhile, the NVPF/HC cell owns the lowest median entropy change among all these chemistries, implying that the effect of reversible (entropic) heat can be large in most of the SOC range. The high entropic heat could be a double–edged sword. In accordance with Damay et al.,[39] the strong entropic cooling of NVPF/HC could buffer the substantial overpotential heat during the fast-charging;

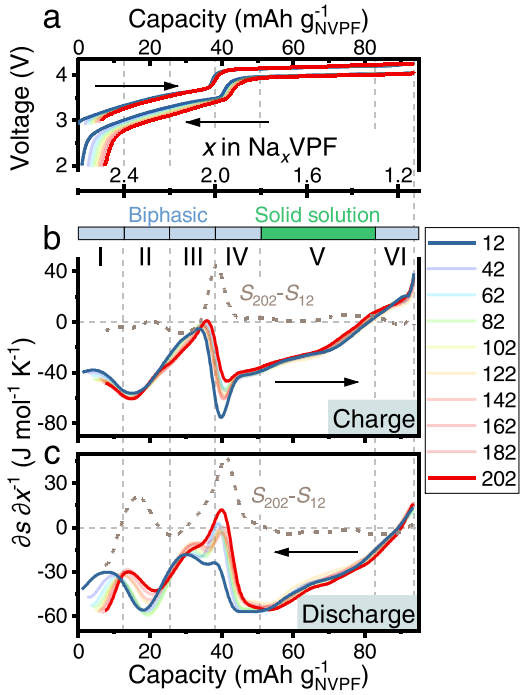

Figure 4. Evolution of entropy profiles upon cell ageing. a-c, The voltage (**a**) and entropy ($\frac{\partial s}{\partial x}$ or equally $\frac{\partial s_+}{\partial x} - \frac{\partial s_-}{\partial x}$, **b,c**) profiles vs capacity at 1 C during the charge (**b**) and discharge (**c**) upon ageing in a 55 °C oven. Note that the curves are aligned at the end of the charge. The arrows in **a-c** indicate the charge/discharge directions. To better understand the complicated variations, we provide another scale relying on the sodium intercalation number, x, in $Na_xV_2(PO_4)_2F_3$ in the space between **a** and **b**. Note that this scale is aligned according to the lost capacity in the higher-voltage plateau. The transition between two plateaus is located at $x = 2.0$. With this scale, we further divide the plots into six regions (I, II, III, IV, V, and VI) according to the reported phase diagram[43] of NVPF from the operando synchrotron XRD. Note that only region V (green) corresponds to a solid-solution reaction, and the others (I-IV and VI, blue) are correlated to biphasic reactions. In each panel, the colours of curves vary from blue to red, with the increasing cycle number from 12 to 202. To simplify the figure, we highlight the curves at 12 and 202 cycles by rendering the others partly transparent. In **a** and **b**, we also computed the difference between the 12th and 202nd cycles in brown dash lines.

however, the strong entropic heating of NVPF/HC will exacerbate the temperature rise of batteries in discharge and thus requires an appropriate design of the cooling system for fast-discharging applications. Interestingly, Wang et al. proposed to elevate the cell temperature to enable extreme fast charging,[40] while too high temperature during fast charging will indeed be troublesome for the safety and reliability of batteries. To ensure this delicate balance between risks of dendrite growth and parasitic reactions, the thermal management for fast charging becomes increasingly essential.

From the sizes of the boxes in Fig. 2b, the spreads of entropic heats rank in the following sequence: $LiCoO_2$/C > NVPF/HC > $LiMn_2O_4$/C > $LiFePO_4$/C > $LiNi_{1/3}Mn_{1/3}Co_{1/3}O_2$/C > $LiNi_{0.8}Co_{0.15}Al_{0.05}O_2$/C. The higher spreading of entropic heat implies a more dynamic change of entropic heat, which may bring about more complexity to the battery thermal management system.

Entropy profiles of half cells.—To untangle the coupling between NVPF and HC, we first calculated the entropy profiles of HC/Na and NVPF/Na separately by the potentiometric method (Fig. 3), because we could not use optical fiber calorimetry for coin cells due to the small amount of materials. Good repeatability of the entropy results was seen by duplicate cells and different temperatures (Fig. S3), despite the presence of uncertainties in some regions such as the sloping voltage region of HC/Na. This sloping voltage region of HC/Na was previously ascribed to the Na ad- and de-sorption on disordered graphene sheets, while the plateau region was correlated to the filling of Na into the carbon mesopores.[41] Given the decrease and then increase of $\frac{\partial s}{\partial x}$ profile in the sloping-voltage region of HC/Na (Fig. 3b), we agree with Mercer et al.[42] that there may be an intermediate stage where both Na adsorption and pore filling happen (purple region, Figs. 3a, 3b). Interestingly, the entropy hysteresis is also captured in this sloping voltage region of HC/Na (Fig. 3). Mckinnon et al. also found a very similar entropy hysteresis in $Li_xMo_6Se_8$ near $x = 2.7$, which they attributed to the path-dependent smearing effects from neighbor transitions.[31] The entropy profile of the pore-filling region in Fig. 3b has a similar shape to Fig. 1b, suggesting the pore-filling process can be modeled by the mean-field lattice gas theory.[31]

In comparison to HC/Na, the magnitude of the entropy profile of NVPF/Na is higher (up to −100 vs −15 J mol^{-1} K^{-1}), implying the varying entropy profiles of the full cell may be more sensitive to the changes in NVPF side. According to the phase diagram of NVPF reported by the synchrotron XRD[43] (Fig. 3c, inset), there is a solid-solution reaction between $x = 1.8$ and 1.3 in Na_xVPF, where the entropy profile is similar to that of Fig. 1b. Turning to the biphasic regions[43] as reported by XRD, $\frac{\partial s}{\partial x}$ plateaus are visible in a few regions, including $x = 3.0$–2.6, $x = 2.0$–1.8, and $x = 1.3$–1.1, indicating first-order transitions similar to that of Fig. 1d. Instead, the $\frac{\partial s}{\partial x}$ profiles in other biphasic domains vary substantially, which may be explained by the higher order phase transitions[31,32] (e.g., the second-order transitions[32,44] in Li_xCoO_2 around $x = 0.5$) or the smearing effect from neighbouring transitions.[31] The entropy profiles of these regions also possess hysteresis, part of which stems from the self-discharge (Fig. S4). In fact, the coulomb counting did not correspond to a "true" derived x because of the parasitic reaction at high voltage. Even after correction of self-discharge (Fig. S4), the remaining hysteresis of NVPF/Na (Fig. 3c) is consistent with the peak shifts in the dV/dQ plots,[17,45] indicating the presence of metastable pathways during the (de-)sodiation of NVPF.

Note that entropy is a state function, and the hysteresis of entropy profiles in Figs. 3b, 3c may imply the presence of metastable and asymmetrical reaction pathways during the charge and discharge.

Entropy implications on cycling ageing.—Figure 4 shows the $\frac{\partial s}{\partial x}$ profiles of sodium-ion 18650 NVPF/HC batteries upon cycling ageing. Variations of $\frac{\partial s}{\partial x}$ profiles are spotted in Figs. 4b, 4c, indicating the complex intercalation mechanisms in NVPF/HC chemistry. To clarify the intercalation mechanism, we also attached the reported phase diagram[43] of NVPF above Fig. 4b with each phase domain referenced by Roman numbers (I-VI in Fig. 4b). They are mostly biphasic phase transition regions, except for region V (shaded in green) with the monophasic (solid solution) reactions.

In order to clearly see the contributions of NVPF and HC to the full-cell entropy profiles, we plotted the half-cell results against the full-cell ones at 12th and 202nd cycles in Fig. 5. Note that we have mimicked Dahn's dV/dQ freeware[46] to estimate the internal balancing, according to the equations:[46] $Q_P = q_P m_P + \delta_P$ and $Q_N = q_N m_N + \delta_N$, where Q_i, q_i, m_i, and δ_i are capacity (mAh), specific capacity (mAh g^{-1}), active material mass (g), and slippage (mAh g^{-1}), respectively, of positive ($i = P$) and negative ($i = N$) electrodes. Accordingly, the half-cell entropy results were fitted (orange and purple scatters, Figs. 5b, 5c, 5e, 5f) by firstly aligning the dip positions of NVPF/Na to the full-cell ones and then tuning the parameters (m_P, m_N, δ_P, δ_N). The slippage of HC/Na is ∼7.5 mAh g_{NVPF}^{-1} from 12th to 202nd cycles according to the fitting, while the fitting does not suggest considerable changes of other parameters (m_P, m_N, δ_P). According to the equation, $\frac{\partial s}{\partial x} = \frac{\partial s_+}{\partial x} - \frac{\partial s_-}{\partial x}$, we also reconstructed NVPF/HC entropy profiles (grey lines, Figs. 5b, 5c), whose shapes are largely consistent with the estimated 18650 full-cell data (blue lines, Figs. 5b, 5c). The remaining

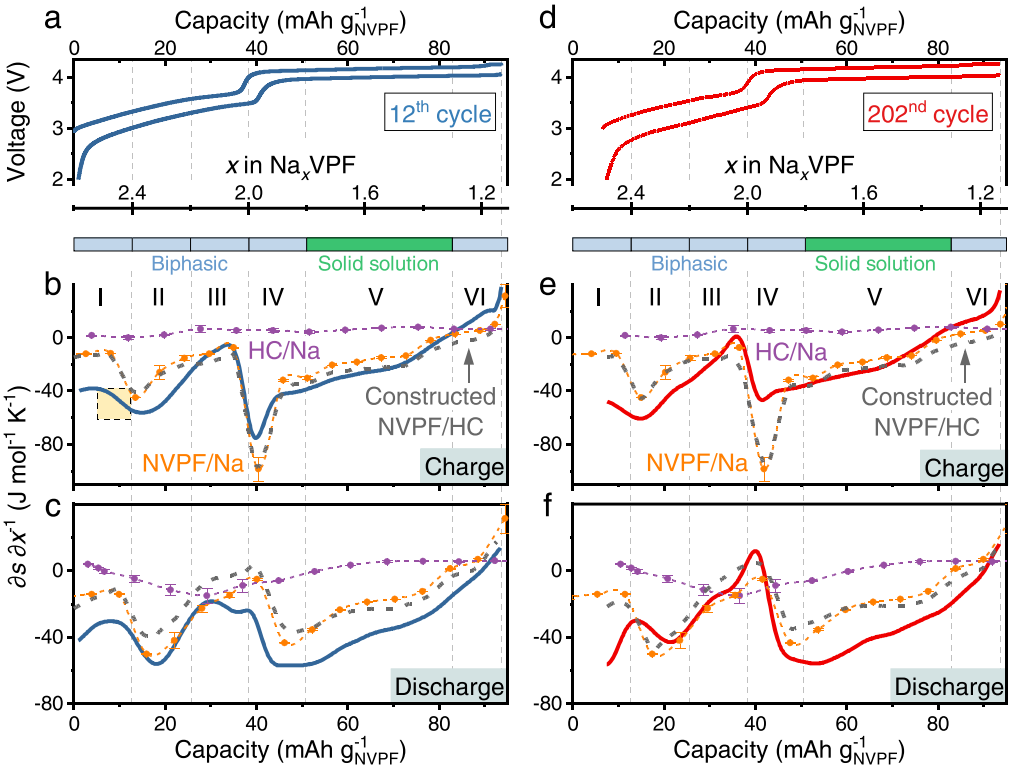

Figure 5. Evolution of entropy profiles upon cell ageing. a-e, The voltage (**a,d**) and entropy ($\frac{\partial s}{\partial x}$ or equally $\frac{\partial s_+}{\partial x} - \frac{\partial s_-}{\partial x}$, **b,c,e,f**) profiles vs capacity at 1 C during the charge (**b,e**) and discharge (**c,f**) at the 12th (**a-c**) and 202nd (**d-f**) cycle in a 55 °C oven. We also plotted the entropy profiles of NVPF/Na (orange, after removing the self-discharge shift, see Fig. S4) and HC/Na (purple), whose capacities were re-scaled and shifted by aligning the dip positions of NVPF/Na and considering the slippage of HC/Na. Note that the fittings of charge and discharge share one set of parameters in the same cycle. The reconstructed entropy profile of NVPF/HC (grey line) was computed by subtracting the entropy of HC/Na from that of NVPF/Na.

differences may originate from the different cell configurations, the relatively low resolution of the potentiometric method, the smearing effects[31] at a high rate of 1 C, and also the errors of the calorimetric method arising from a few assumptions as discussed above in Introduction and Experimental.

Going into the details, the HC/Na entropy is not only marginal in amplitude but also flat with no visible peaks during the charge (purple line, Fig. 5b). In contrast, the entropy profiles of NVPF/Na are intense and full of features including peaks, valleys, and plateaus (orange line, Fig. 5b), which are associated with the stepwise biphasic and solid-solution (de-)sodiation mechanisms in NVPF[43] (inset between Figs. 5a, 5b). Consequently, the entropy of HC seems negligible to the full-cell entropy during the charge; however, during the discharge, the entropy of HC/Na shows a large dip centered around 30 mAh g_{NVPF}^{-1} (purple line, Fig. 5c), which noticeably affects the shape of whole-cell entropy. Equally, the entropy profile of NVPF/Na during the discharge is informative with plenty of features (orange line, Fig. 5c).

Turning to the full-cell results, we first discussed the relatively pristine $\frac{\partial s}{\partial x}$ profiles at 12th cycle (blue lines in Figs. 5b, 5c). Starting from the whole picture, the $\frac{\partial s}{\partial x}$ shapes of charge and discharge are not well aligned to each other at the lower-voltage regions (I, II in Figs. 5b, 5c): There is a right shift of the discharge by ~3 mAh g_{NVPF}^{-1} when compared to that of charge. Because the irreversible capacity of the 12th cycle is < 1 mAh g_{NVPF}^{-1} (Fig. 5a), this shift does not stem from the slippage due to irreversible reactions. A similar shift was observed in the $\frac{\partial s}{\partial x}$ profile of lithium- and manganese-rich layered transition metal oxides[34] by Gasteiger et al. They found that this path dependence appeared only as a function of SOC and disappeared as a function of OCV.[34] Since the configurational entropy (S_{conf}) of intercalants is dependent on SOC,[34] they further attributed this shift to the prominence of changes in vibrational entropy (S_{vib}) of the host lattice during phase transition. To assess this hypothesis in NVPF/HC chemistry, we plotted the pristine $\frac{\partial s}{\partial x}$ profiles at the 12th cycle vs OCV in Fig. 6c. Nice superimposition is found between the charge and discharge curves except for minor entropy hysteresis at OCV < 3.2 V, supporting the possible S_{vib}-dominant mechanism.[34] Indeed, this hysteresis could also stem from the smearing from different preceding transitions when the reaction direction was reversed, as Mckinnon et al. proposed[31] in $Li_xMo_6Se_8$ near $x = 2.7$.

We then analyzed the data region by region. Through region I of Figs. 5b, 5c that corresponds to a phase transition between orthorhombic Na_3VPF and $Na_{2.4}VPF$, the peak of $\frac{\partial s}{\partial x}$ with the decreasing $\frac{\partial s}{\partial x}$ between $x = 2.5$ and 2.4 (yellow region, Fig. 5b) concurs with the intermediate (probably metastable) states near $x = 2.5$ as disclosed by previous synchrotron XRD studies.[43] This peak shape is in contrast with the valley observed in region II (Figs. 5b, 5c), which corresponds to the transition between $Na_{2.4}VPF$ and tetragonal $Na_{2.2}VPF$. To account for the existence of a peak and a valley in the entropy profile for regions I and II, respectively, we will refer to early synchrotron XRD studies by Bianchini et al.[43] The authors found that $Na_{2.4}VPF$ possessed a superstructure due to the possible ordering of sodium and/or vanadium ions, while $Na_{2.2}VPF$ exhibited a disordered arrangement of sodium ions. Cation ordering and disorder unquestionably influence entropy. Given the observations in regions I and II, the transition from disordered ($Na_{2.2}VPF$) to ordered ($Na_{2.4}VPF$) cation arrangements would have a $\frac{\partial s}{\partial x}$ valley, while the transition from ordered $Na_{2.4}VPF$ to Na_3VPF gives rise to a $\frac{\partial s}{\partial x}$ peak. We are confident about this assignment because the ordered cations should have a relatively negative configurational entropy, explaining the shapes of $\frac{\partial s}{\partial x}$. Meanwhile, the thermal entropy

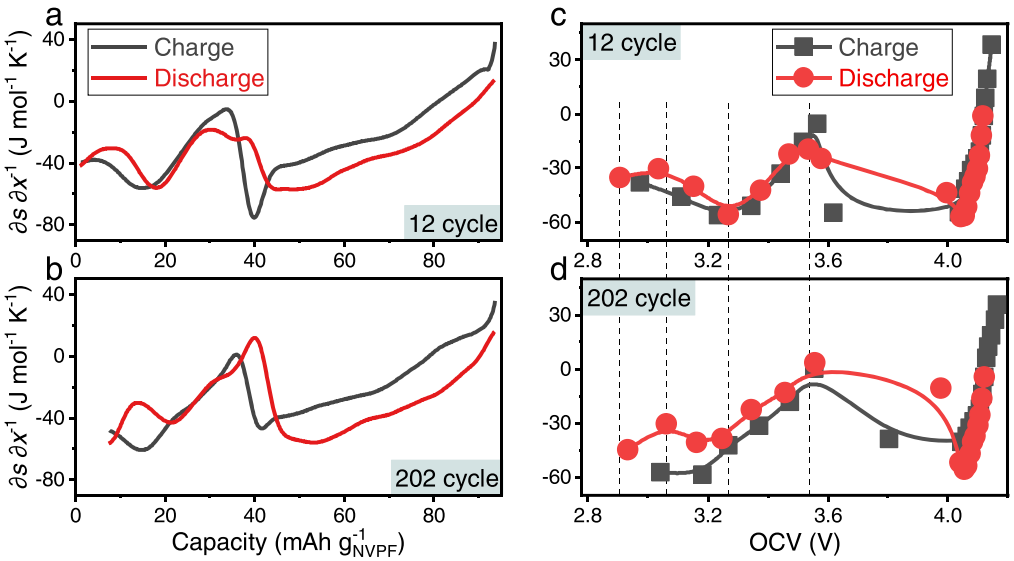

Figure 6. $\frac{\partial s}{\partial x}$ hysteresis of the 18650 full cells. a,b, The $\frac{\partial s}{\partial x}$ profiles vs capacity at 12th (a) and 202nd (b) cycles during the charge (black) and discharge (red). c,d, The $\frac{\partial s}{\partial x}$ profiles vs OCV at the 12th (c) and 202nd (d) cycles during the charge (black squares) and discharge (red circles). Note that the OCV was extracted from the GITT test by directly taking the voltage after long-time relaxation without any computations. Solid lines are provided by B-spline as a guide to the eyes. Dash lines are references to examine the possible shifts between the curves.

may be the reasons for the negative $\frac{\partial s}{\partial x}$ in both regions I and II. The correlation between $\frac{\partial s}{\partial x}$ peak/valley and cation ordering is validated in region III of Figs. 5b, 5c): a $\frac{\partial s}{\partial x}$ peak is observed in the phase transition between Na_2VPF (possessing a superstructure with sodium and vanadium ordering)[43] and $Na_{2.2}VPF$ (with a disordered Na^+ arrangement). These encouraging results suggest the possibility of tracking the cation ordering by the entropy profile.

Turning to region IV (Figs. 5b, 5c), the valley of $\frac{\partial s}{\partial x}$ from Na_2VPF to $Na_{1.8}VPF$ is again associated with the sodium and vanadium cation disordering in $Na_{1.8}VPF$ structure[43] together with the metastable phases[43] observed around $x = 2.0$ and 1.9. Meanwhile, the plateau between $x = 1.9$ and 1.8 accords with the first-order transition confirmed by the synchrotron XRD.[43] As expected, the $\frac{\partial s}{\partial x}$ profile in the region V (Figs. 5b, 5c) shows a similar shape to that of Fig. 1b that is characteristic of a monophasic reaction of NVPF.[43] In biphasic region VI (Figs. 5b, 5c), the sloping $\frac{\partial s}{\partial x}$ of full cell originates partly from the sloping $\frac{\partial s}{\partial x}$ tail of HC (Fig. 3b), while the relatively high rate of 1 C may also impose the deviation from the equilibrium.

Finally, with respect to ageing, we mainly compare the changes between two extremes, namely, the 12th (blue lines in Figs. 4b, 4c) and 202nd (red lines in Figs. 4b, 4c) cycles. The disappearance of the $\frac{\partial s}{\partial x}$ peak in the region I upon cycling ageing well reflects the lost capacity of Na_3VPF-$Na_{2.4}VPF$ transition, likely due to the loss of sodium inventory and the slippage of HC, as verified by the entropy fitting in Fig. 5e. On the contrary, during discharge, the $\frac{\partial s}{\partial x}$ peak remains while penetrating into region II. This difference and hysteresis between charge and discharge curves at the 202nd cycle are still seen in the $\frac{\partial s}{\partial x}$ profiles against OCV (Figs. 6b, 6d). The $\frac{\partial s}{\partial x}$ peak during the discharge (Fig. 4c, red line) in regions I and II coincidently takes place at around 3 V (Fig. 4a), where Desai et al. reported a possible redox reaction of dissolved vanadium[47] from NVPF. The hysteresis may pertain to the dissolution of vanadium.[47]

In region III, during the charge, the left side of $\frac{\partial s}{\partial x}$ peak becomes less steep (Fig. 4b, blue and red lines). A similar slope change is seen in the discharge of region III with a more significant change of $\frac{\partial s}{\partial x}$ around $x = 2$ (brown dash line, Fig. 4c). Indeed, the structural change around $x = 2$ will also influence the $\frac{\partial s}{\partial x}$ shapes in regions III and IV (Figs. 4b, 4c). Notably, the $\frac{\partial s}{\partial x}$ plateau at the 12th cycle during the discharge (Fig. 4c, blue line) of region IV gradually tilts with cycle number (Fig. 4c, red line), implying the continuous loss of the thermodynamically favored first-order transition and the increasing appearance of metastable phases. Turning to regions V and VI (Figs. 4b, 4c), negligible changes of $\frac{\partial s}{\partial x}$ profiles resonate with the relatively small capacity degradation in the higher-voltage plateau (Fig. 4a). Overall, the above results demonstrate the possibility of entropy profiles to track structure-related ageing in commercial cells.

Entropy as an indicator of battery's health.—In addition to the in-depth analysis mentioned above, the next question is how entropy can benefit practical applications, such as estimating battery SOH. Without complicating the work by the feature engineering techniques of artificial intelligence, we simply relied on the data and region definitions as shown in Fig. 4 and calculated the average entropies ($\frac{\partial s}{\partial x}$) of the six regions of different cycles. To easily compare the changes in different regions, the changes of average entropies relative to that of the 12th cycle are plotted as a function of cycle number in Figs. 7a, 7b. The average entropies of regions I and IV during charge and of regions I, II, II, and IV during the discharge visibly vary during the cycling ageing. These variations again indicate the sensitivity of entropy to the degradation of batteries.

To further investigate the potential of entropy features as fingerprints for detecting battery health, we took the discharge capacity and calculated the ΔV (difference between the average charge and discharge voltages as a proxy for internal impedance of each cycle (that is, 12th, …, 202nd cycles) as the resistance state of health (SOHR). The states of the batteries and the average entropies in the different regions can thus be linked via the cycle number, and their Pearson coefficients could be calculated to measure their linear correlations; see the examples of the region IV during discharging (Figs. 7c, 7d). Remarkably, Pearson coefficients above 0.9 or below −0.9 are found in a few combinations (Fig. 7e), implying the very strong linear correlations between entropies and the SOH (or SOHR). To further solidify this conclusion, the entropy profiles were aligned at the start rather than the end of the charge (Fig. S5).

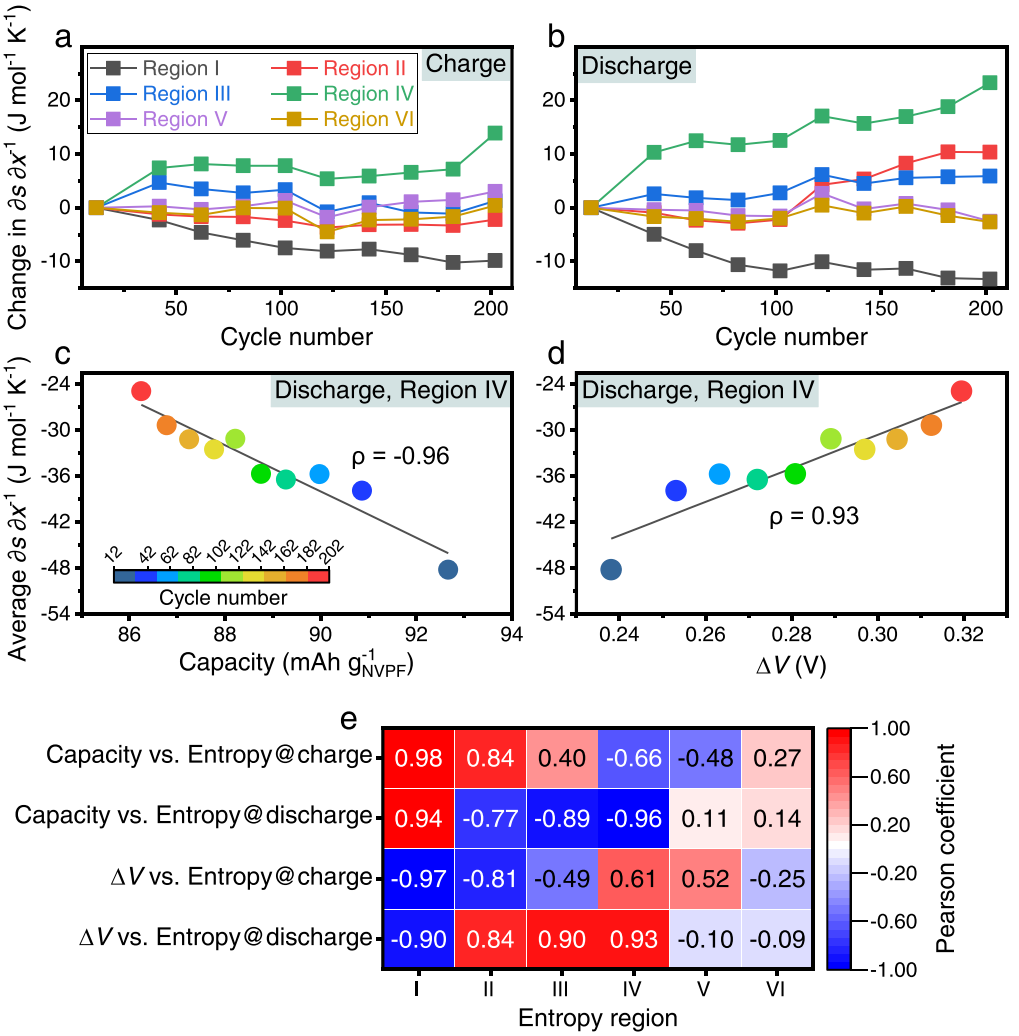

Figure 7. Entropy fingerprint for detecting the states of the battery. a,b, The change of average entropy ($\frac{\Delta S}{\Delta x}$) of the six regions (see Fig. 4) relative to that of the 12th cycle as a function of cycle number during the charge (a) and discharge (b). c,d, The correlations between the average entropy of region IV during the charge and the discharge capacity (**c**) or ΔV (d). Note that this region is shown here to give an example to compute the Pearson coefficients. The colours of scatters vary from blue to red with the increasing cycle number from 12 to 202. **e**, The Pearson coefficients between the discharge capacity (or the ΔV, the bottom two rows) and the average entropy of the six regions during the charge (1st and 3rd rows) and discharge (2nd and 4th rows).

High Pearson coefficients were again observed in different regions (Fig. S5), verifying the strong correlations between entropies and the SOH (or SOHR). Thus, the entropy features have great potential as indicators for the states of batteries. Remarkably, the features in the region I showed the largest Pearson coefficients and, therefore, the strongest linear correlations to the states of batteries in comparison to other regions. This can be immensely useful for quickly diagnosing batteries for the purpose of classification or quality control, which has been proved in another work under preparation.

Conclusions

We demonstrate the feasibility of using FBG sensors and optical fiber calorimetry for operando monitoring of the entropy profiles of commercial sodium-ion cells. By directly comparing the entropy profiles of NVPF/HC with some typical lithium-ion chemistries, we highlight the possible benefits of high entropic heat of NVPF/HC for fast-charging applications, though the high entropic heat could be a troublemaker in the fast-discharging scenarios. Turning to battery ageing, this work not only extends the entropy analyses of ageing from lithium-ion to sodium-ion chemistries but also demonstrates the advantages of the calorimetric method[12] in operando monitoring of battery ageing. Lastly, we capture the features of entropy in different phase transition regions and prove their strong correlations with the SOH and SOHR of the batteries.

Thermodynamic analyses are useful to batteries in terms of thermal management and safety. Moreover, the high sensitivity of entropy to the structural variations of the system does offer additional ways to monitor and understand battery ageing. Consequently, the dynamics of entropy profiles of different chemistries under diverse working conditions deserve further explorations, where metastable reaction pathways are of great interest. To this end, a more reliable, automated, and powerful fiber-optic calorimetric method should be developed in both hard- and soft-wares. In particular, the applications of the calorimetric method are still largely limited to commercial cells, and its success in emerging chemistries (e.g., aqueous or solid-state batteries) necessitates new and adaptative setups and calibration methods. Overall, we see a myriad of opportunities that the combination of thermodynamics and optical fiber sensors could create for battery application, and the continued prosperity of the battery industry and research will require interdisciplinary expertise and cooperation.

Acknowledgments

We thank TIAMAT for kindly providing the NVPF/HC 18650 cells. We acknowledge BATTERY 2030+ funded by the European

Union's Horizon 2020 research and innovation program under grant agreement No. 957213, and the funding from the International Balzan Prize Foundation via the 2020 Balzan Prize to Jean-Marie Tarascon. J.H. is also indebted to the National Natural Science Foundation of China (No. 52207230 and 92372109), the Hong Kong University of Science and Technology (Guangzhou) startup grant (G0101000062), the Project of Hetao Shenzhen-Hong Kong Science and Technology Innovation Cooperation Zone (HZQB-KCZYB-2020083), and the Guangzhou-HKUST(GZ) Joint Funding Program (No. 2023A03J0003 and No. 2023A03J0103).

Author Contributions

J. H. and J.-M. T. conceived the idea and designed the experiments. J.H. performed the electrochemical and optical measurements together with the data analysis. J.H. did the thermodynamics analysis with the help of C. D. Additionally, P. D. conducted the entropy estimations using the potentiometric method. Lastly, J. H. and J.-M. T. wrote the paper with the contributions from C. D.

ORCID

Jiaqiang Huang https://orcid.org/0000-0001-8250-228X
Charles Delacourt https://orcid.org/0000-0001-5241-5441

References

1. J. Huang, S. T. Boles, and J.-M. Tarascon, *Nat. Sustain.*, **5**, 194 (2022).
2. X. Lu, J.-M. Tarascon, and J. Huang, *eTransportation*, **14**, 100207 (2022).
3. J. M. Sherfey and A. Brenner, *J. Electrochem. Soc.*, **105**, 665 (1958).
4. H. F. Gibbard, *J. Electrochem. Soc.*, **125**, 353 (1978).
5. J. Dahn, W. McKinnon, J. Murray, R. Haering, R. McMillan, and A. Rivers-Bowerman, *Phys. Rev. B: Condens. Matter Mater. Phys.*, **32**, 3316 (1985).
6. A. Yamada, H. Koizumi, S.-I. Nishimura, N. Sonoyama, R. Kanno, M. Yonemura, T. Nakamura, and Y. Kobayashi, *Nat. Mater.*, **5**, 357 (2006).
7. G. Assat, S. L. Glazier, C. Delacourt, and J.-M. Tarascon, *Nat. Energy*, **4**, 647 (2019).
8. K. Maher and R. Yazami, *J. Power Sources*, **247**, 527 (2014).
9. H. J. Kim, Y. Park, Y. Kwon, J. Shin, Y.-H. Kim, H.-S. Ahn, R. Yazami, and J. W. Choi, *Energy Environ. Sci.*, **13**, 286 (2020).
10. M. Kim, H. Kim, I. Kim, B. Chang, and J. W. Choi, *Proc. Natl. Acad. Sci. U. S. A.*, **119**, e2211436119 (2022).
11. M. E. Wojtala, A. A. Zülke, R. Burrell, M. Nagarathinam, G. Li, H. E. Hoster, D. A. Howey, and M. P. Mercer, *J. Electrochem. Soc.*, **169**, 100527 (2022).
12. J. Huang et al., *Nat. Energy*, **5**, 674 (2020).
13. K. E. Thomas and J. Newman, *J. Electrochem. Soc.*, **150**, A176 (2003).
14. L. Downie, S. Hyatt, and J. Dahn, *J. Electrochem. Soc.*, **163**, A35 (2016).
15. L. Downie and J. Dahn, *J. Electrochem. Soc.*, **161**, A1782 (2014).
16. S. Glazier, R. Petibon, J. Xia, and J. Dahn, *J. Electrochem. Soc.*, **164**, A567 (2017).
17. J. Huang, C. Delacourt, P. Desai, C. Gervillié-Mouravieff, L. Albero Blanquer, R. Tan, and J.-M. Tarascon, *J. Electrochem. Soc.*, **170**, 090510 (2023).
18. J. Huang, X. Han, F. Liu, C. Gervillié, L. A. Blanquer, T. Guo, and J.-M. Tarascon, *Energy Environ. Sci.*, **14**, 6464 (2021).
19. L. Albero Blanquer, F. Marchini, J. R. Seitz, N. Daher, F. Bétermier, J. Huang, C. Gervillié, and J.-M. Tarascon, *Nat. Commun.*, **13**, 1153 (2022).
20. J. Bonefacino et al., *J. Electrochem. Soc.*, **169**, 100508 (2022).
21. J. Huang, L. A. Blanquer, C. Gervillie, and J.-M. Tarascon, *J. Electrochem. Soc.*, **168**, 060520 (2021).
22. C. Gervillié-Mouravieff et al., *Nat. Energy*, **7**, 1157 (2022).
23. P. Desai, J. Huang, H. Hijazi, L. Zhang, S. Mariyappan, and J. M. Tarascon, *Adv. Energy Mater.*, **11**, 2101490 (2021).
24. C. Forgez, D. V. Do, G. Friedrich, M. Morcrette, and C. Delacourt, *J. Power Sources*, **195**, 2961 (2010).
25. K. E. Thomas, C. Bogatu, and J. Newman, *J. Electrochem. Soc.*, **148**, A570 (2001).
26. Y. Reynier, R. Yazami, and B. Fultz, *J. Electrochem. Soc.*, **151**, A422 (2004).
27. G. Dudley, K. Cheung, and B. Steele, *J. Solid State Chem.*, **32**, 269 (1980).
28. C. J. Wen and R. A. Huggins, *J. Electrochem. Soc.*, **128**, 1181 (1981).
29. P. J. Osswald, M. D. Rosario, J. Garche, A. Jossen, and H. E. Hoster, *Electrochim. Acta*, **177**, 270 (2015).
30. D. R. Gaskell, *Introduction to the Thermodynamics of Materials* (Taylor and Francis, New York) 4th ed. (2003).
31. W. R. McKinnon, J. R. Dahn, J. J. Murray, R. R. Haering, R. S. McMillan, and A. H. Rivers-Bowerman, *J. Phys. C: Solid State Phys.*, **19**, 5135 (1986).
32. Y. Reynier, J. Graetz, T. Swan-Wood, P. Rez, R. Yazami, and B. Fultz, *Phys. Rev. B: Condens. Matter Mater. Phys.*, **70**, 174304 (2004).
33. S. Schlueter, R. Genieser, D. Richards, H. E. Hoster, and M. P. Mercer, *Phys. Chem. Chem. Phys.*, **20**, 21417 (2018).
34. F. Friedrich, S. Pieper, and H. A. Gasteiger, *J. Electrochem. Soc.*, **168**, 120502 (2021).
35. M. Farkhondeh, M. Pritzker, M. Fowler, M. Safari, and C. Delacourt, *Phys. Chem. Chem. Phys.*, **16**, 22555 (2014).
36. H. L. Smith et al., *Nat. Phys.*, **13**, 900 (2017).
37. V. V. Viswanathan, D. Choi, D. Wang, W. Xu, S. Towne, R. E. Williford, J.-G. Zhang, J. Liu, and Z. Yang, *J. Power Sources*, **195**, 3720 (2010).
38. N. Damay, C. Forgez, M.-P. Bichat, and G. Friedrich, *J. Power Sources*, **332**, 149 (2016).
39. N. Damay, R. Recoquillé, H. Rabab, J. Kozma, C. Forgez, A. El Mejdoubi, and K. El Kadri Benkara, *J. Power Sources*, **581**, 233460 (2023).
40. X.-G. Yang, T. Liu, Y. Gao, S. Ge, Y. Leng, D. Wang, and C.-Y. Wang, *Joule*, **3**, 3002 (2019).
41. B. Zhang, C. M. Ghimbeu, C. Laberty, C. Vix-Guterl, and J.-M. Tarascon, *Adv. Energy Mater.*, **6**, 1501588 (2016).
42. M. P. Mercer, S. Affleck, E. M. Gavilán-Arriazu, A. A. Zülke, P. A. Maughan, S. Trivedi, M. Fichtner, A. Reddy Munnangi, E. P. M. Leiva, and H. E. Hoster, *ChemPhysChem*, **23**, e202100748 (2022).
43. M. Bianchini, F. Fauth, N. Brisset, F. Weill, E. Suard, C. Masquelier, and L. Croguennec, *Chem. Mater.*, **27**, 3009 (2015).
44. J. N. Reimers and J. R. Dahn, *J. Electrochem. Soc.*, **139**, 2091 (1992).
45. G. Yan, R. Dugas, and J.-M. Tarascon, *J. Electrochem. Soc.*, **165**, A220 (2018).
46. H. M. Dahn, A. J. Smith, J. C. Burns, D. A. Stevens, and J. R. Dahn, *J. Electrochem. Soc.*, **159**, A1405 (2012).
47. P. Desai, J. Forero-Saboya, V. Meunier, G. Rousse, M. Deschamps, A. Abakumov, J.-M. Tarascon, and S. Mariyappan, *Energy Storage Mater.*, **57**, 102 (2022).